Applied Physics Letters ARTICLE pubs.aip.org/aip/apl

Nano-Raman imaging of monolayer MoS_2 nanoribbons

Cite as: Appl. Phys. Lett. **128**, 203102 (2026); doi: 10.1063/5.0321304
Submitted: 6 January 2026 · Accepted: 8 April 2026 ·
Published Online: 18 May 2026

View Online Export Citation CrossMark

Andrey Krayev,[1,a)] Tara Peña,[2] Anton E. O. Persson,[2] Kathryn Neilson,[2] Anh Tuan Hoang,[3] Andrew J. Mannix,[3,4] and Eric Pop[2,3,5,6]

AFFILIATIONS

[1]HORIBA Scientific, Novato, California 94949, USA
[2]Department of Electrical Engineering, Stanford University, Stanford, California 94305, USA
[3]Department of Materials Science and Engineering, Stanford University, Stanford, California 94305, USA
[4]Stanford Institute for Materials and Energy Sciences, SLAC National Accelerator Laboratory, Menlo Park, California 94025, USA
[5]Precourt Institute for Energy, Stanford University, Stanford, California 94305, USA
[6]Department of Applied Physics, Stanford University, Stanford, California 94305, USA

Note: This paper is part of the Special Topic, Advances in Inelastic Light Scattering Spectroscopies.
[a)]**Author to whom correspondence should be addressed:** andrey.krayev@horiba.com

ABSTRACT

Two-dimensional semiconductors are promising candidates for next-generation electronics. However, characterizing these materials at technologically relevant dimensions remains underexplored. Here, we use tip-enhanced Raman spectroscopy (TERS) to map lithographically-patterned monolayer MoS_2 nanoribbons down to 50 nm widths. The surface sensitivity of TERS enables direct nanoscale assessment of the MoS_2 surface after a vacuum annealing procedure that removes resist residues. Subsequently, we find a consistently strong TERS response across the nanoribbon, indicating good quality MoS_2 and a clean interface to the Au substrate. The good spatial resolution of TERS (down to ~10 nm) uncovers small, 50–100 nm regions of inhomogeneities, likely arising from the growth process with a higher intensity and redshifted 2LA(M) peak. We also find a 0.5 cm^{-1} redshift of the A_1' mode at nanoribbon edges, consistent with a fixed negative charge. Our study highlights how advanced nanoscale metrology can be leveraged for future devices and fabrication process optimization.

Raman spectroscopy is an optical, nondestructive technique to inspect composition, strain, doping, and defects in a variety of materials.[1–4] However, conventional Raman spectroscopy is at the mercy of the diffraction limit of light; thus, the subsequent Raman analysis is a convolution of nanoscale effects averaged over the ~1 μm laser spot size. To bypass this limitation, tip-enhanced Raman spectroscopy (TERS) has been proposed for nanoscale imaging, where a metallic tip enhances light signals from plasmonic fields. The spatial resolution of TERS imaging can routinely reach a few tens of nanometers under ambient conditions and can be improved to the sub-nanometer range under ultrahigh vacuum and cryogenic conditions.[5,6]

Tip-enhanced Raman and photoluminescence spectroscopy[7] have enabled nanoscale insights into two-dimensional (2D) materials[8–17] and their heterostructures,[18,19] including nanoscale inhomogeneities and defects. The strongest TERS enhancement and highest spatial resolution are obtained in the "gap-mode" configuration, when a thin sample (a few nanometers or less) is sandwiched between a sharp, plasmonic TERS probe and a metallic substrate. The substrate should either support the plasmon resonances in a similar spectral range as the probe or at least be a good, low loss mirror in that spectral range.[20] To prepare 2D semiconductor samples for gap-mode TERS imaging, samples can be transferred off their original substrate using a gold or silver film, which then becomes the substrate for TERS probing.[21]

Monolayer transition metal dichalcogenides (TMDs) are 2D semiconductors with potential for nanoscale logic transistors, owing to their good charge carrier mobility even in a monolayer material[22–24] (~6 Å) and improved robustness to short-channel effects.[23] As a result, they have been featured on technology roadmaps for next-generation gate-all-around nanosheet transistors.[25] Among TMDs, monolayer MoS_2 transistors have seen the most progress, with recent demonstrations of good electrical contacts,[24,26] doping schemes,[27] and low-temperature synthesis.[28,29] However, most experimental studies have focused on devices with micrometer-scale channel widths, whereas

high-density nanoscale transistors[30] require channel dimensions (both length and width) well below 100 nm. At such scales, edge states, material inhomogeneities, and fabrication-induced disorder[31] could influence electronic properties and contribute to device-to-device variability. Thus, understanding the impact of reducing the TMD dimension is critical, and nanoscale materials characterization techniques are therefore key when evaluating 2D nanoribbon quality prior to device fabrication and electrical testing.

In this study, we use TERS to investigate monolayer MoS_2 nanoribbons of widths below 100 nm, aiming to provide insight into the causes of electrical device-to-device variation. The nanoribbons used in this work are prepared similarly to lithographically patterned monolayer devices recently studied with good electrical performance.[32] In brief, continuous monolayer MoS_2 films were first grown at 750 °C onto 300 nm SiO_2 on Si substrates [Fig. 1(a)] via solid source chemical vapor deposition (CVD).[33] The monolayer nature of the samples was confirmed through photoluminescence, atomic force microscopy (AFM), and optical contrast approaches.[32] These films were then coated with resist for electron-beam lithography (ARP 6200.04, CSAR 62), patterned into ∼1 μm long nanoribbons with widths below 100 nm, and dry-etched with XeF_2 [Fig. 1(b)]. The MoS_2 nanoribbons were designed in a "dumbbell" structure, where contact regions are much wider (∼1 μm) than the nanoribbon channel, to assist the samples' mechanical stability during processing. After etching, the resist was removed in Remover PG, followed by acetone and isopropyl alcohol (IPA) rinses. We found that solvent cleaning alone was not sufficient, because some resist residues remain, hindering proper TERS enhancement [Fig. 1(c)]; thus, in this manuscript we explore implementing an overnight anneal at 250 °C in $\sim 10^{-5}$ Torr vacuum for 8 h [Fig. 1(d)].

To probe the nanoribbons by TERS, a 100 nm Au layer is electron-beam evaporated onto the samples [Fig. 1(e)], then flipped and placed onto a new substrate [Fig. 1(f)], as described in previous work.[21] In this configuration, gap-mode TERS conditions are met as the monolayer MoS_2 is sandwiched between the plasmonic TERS probe and the Au substrate [Figs. 1(g) and 1(h)]. After the vacuum annealing procedure illustrated in Fig. 1(d), we can resolve the prominent peaks of the monolayer MoS_2 nanoribbon, as discussed later. We use an excitation laser energy below the optical bandgap (here, 785 nm or ∼1.58 eV) to increase the signal from the out-of-plane (A_1') and M-point phonon modes, like 2LA(M), for monolayer MoS_2.[34] An additional advantage of this laser is the negligible far-field response, which allowed us to skip collection of far-field maps. For proof of concept, we choose a 300 l/mm spectrometer grating, allowing us to obtain higher Raman intensity from the MoS_2 phonon modes and simultaneously investigate Stokes and anti-Stokes peaks. However, this spectrometer grating also introduces more instrumental broadening and sacrifices some spectral resolution (pixel to pixel step is $\sim 2\ cm^{-1}$).

Atomic force microscopy (AFM) and TERS imaging were carried out on a LabRam-Nano AFM-Raman system (HORIBA Scientific). Excitation and collection of the TERS signal were done using the side 100×, 0.7 NA objective (Mitutoyo) inclined at 25° to the sample plane. Gold-coated OMNI-TERS-SNC-Au AFM

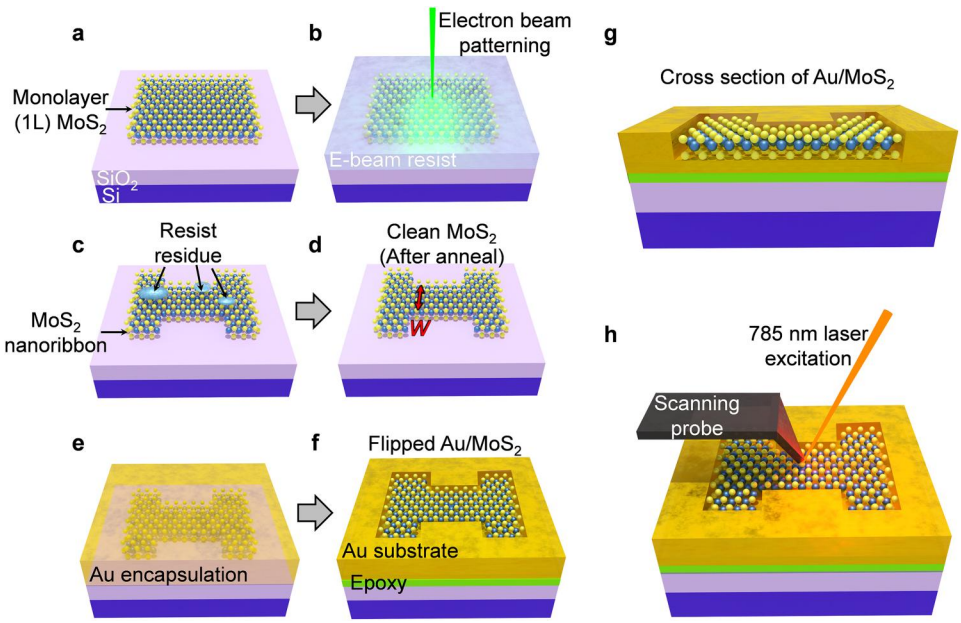

FIG. 1. Schematics of the sample preparation for TERS characterization on lithographically patterned monolayer MoS_2 nanoribbons. (a) Monolayer MoS_2 is grown directly onto SiO_2/Si substrates. (b) Resist is spun onto the sample and then exposed to electron-beam patterning to define the nanoribbon shape, followed by dry etching to obtain the final nanoribbons. (c) After the resist is stripped using solvents, resist residues often remain on the MoS_2 and SiO_2 surfaces. (d) To obtain clean MoS_2 nanoribbons, the sample is annealed under vacuum as described in the main text. *W* denotes the nanoribbon width. (e) Au (100 nm) is electron-beam evaporated onto the sample. The Au/MoS_2 interface is cleaner if the vacuum anneal is employed. (f) The Au/MoS_2 is stripped using the glued transfer wafer (with the MoS_2 upward). (g) Schematic of the final sample, showing the MoS_2 embedded into the Au substrate for gap-mode TERS imaging. (h) Tip-enhanced Raman spectroscopy (TERS) is conducted on the final sample, with a 785 nm laser excitation used in this study.

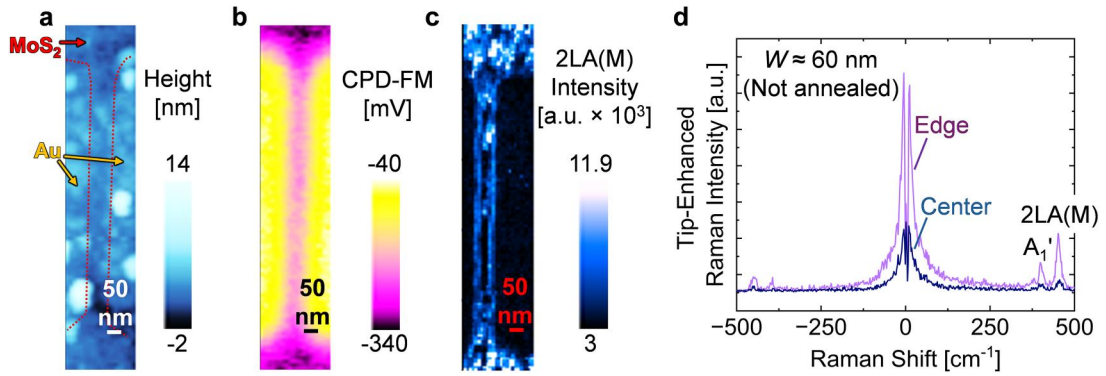

FIG. 2. TERS imaging of MoS_2 nanoribbons prepared without vacuum annealing. (a) Topography and (b) contact potential difference (CPD-FM) image of a MoS_2 nanoribbon ($W \approx 60$ nm) transferred onto Au after solvent cleaning, but without vacuum annealing. (c) Tip-enhanced Raman spectroscopic (TERS) map of the same MoS_2 nanoribbon (250×1200 nm^2 map, 10 nm per pixel), displaying the intensity of the 2LA(M) mode. The intensity is nonuniform across the sample, likely due to resist residue at the Au substrate/MoS_2 interface. (d) Raw TERS spectra of two points on the TERS map, displaying representative spectra from the nanoribbon edges and center of the channel. The nanoribbon center has a lower signal-to-noise ratio, alongside a decrease in intensity of the broad bell centered at 0 cm^{-1}. Conversely, the edges have reasonably strong MoS_2 Raman peaks and higher intensity of the broad bell.

cantilevers (APPNano) were used for both the AFM and TERS characterization. Laser power past the objective was maintained between 100 and 250 μW. The AFM topography and the corresponding contact potential difference (surface potential) images of a Au-transferred nanoribbon with a width of 60 nm from the first batch (without the vacuum annealing) are presented in Figs. 2(a) and 2(b).

AFM topography imaging of the samples from the first batch revealed contamination particles on the Au surface. The contact potential difference (CPD-FM) image collected using a two-pass frequency-modulated version of scanning Kelvin microscopy (SKM-FM) reveals the presence of the nanoribbons, although the spatial resolution of the surface potential image was limited by the tip radius (~50 nm) and the tip-sample distance of ~35 nm during the measurements of the surface potential. The first TERS map was collected over the full length of the nanoribbon and the wider regions at the ends. The TERS map [Fig. 2(c)] shows the distribution of the intensity of the complex 2LA(M) peak at around 451 cm^{-1}, as marked in Fig. 2(d). The out-of-plane (A_1') Raman mode can also be examined in the spectra [Fig. 2(d)], but this peak may experience instrumental broadening and possible splitting caused by the TMD interaction with the Au substrate.[35] Gap-mode TERS with sub-bandgap excitation yields a stronger response for monolayers[34] but preferentially enhances only the out-of-plane and M-point phonon modes. For more sophisticated analysis that would resolve the in-plane E′ mode, allowing estimation of strain,[2] laser excitations closer to or above the optical bandgap of MoS_2 would be required, with higher spectral resolution and longer acquisition times.

In Fig. 2(c), we can clearly see that the intensity of the TERS signal was greatly reduced in the central (across its width) part of the nanoribbon and the effect is well reproducible (i.e., not related to temporal fluctuations) as it can be seen over the whole length of the nanoribbon. When examining the raw TERS spectra from various locations of the map in Fig. 2(d), we observe faint MoS_2 signatures at the center of the nanoribbon, thus excluding the possibility of incomplete nanoribbon transfer (which would result in bare gold in the center). Moreover, we clearly see that the bell-shaped feature next to the excitation laser line at 0 cm^{-1} was greatly reduced over the central area, indicating that the overall gap-mode TERS enhancement went down[36] in the center of the nanoribbon channel. This indicates that resist residue was not entirely removed, accumulating on both the central part of the nanoribbon and on the SiO_2 surface, hindering satisfactory gap-mode TERS conditions. Such resist residues are critical to remove, as they can ultimately degrade contact resistances and/or the electrostatic control of gate stacks in 2D devices.

The "bright edge-dim center" pattern was consistently present in all TERS maps collected over the nanoribbons from the first batch (solvent cleaned without vacuum anneal). To test our hypothesis on the incomplete resist removal, the second batch was fabricated (on Si/SiO_2), this time with an additional overnight vacuum anneal (250 °C at ~10^{-5} Torr for 8 h) intended to remove remaining resist and adsorbates from the MoS_2 surface. After this additional step, the nanoribbons were coated with Au and stripped from the SiO_2 growth substrate like the first batch.

For this second vacuum-annealed batch, the topography map in Fig. 3(a) provides clear contrast between the nanoribbons and Au [compared to Fig. 2(a)]. TERS maps acquired with the same 785 nm excitation laser as before show that the dim central region was not present here, and the TERS response was mostly uniform across the nanoribbon width [compare Fig. 3(b) with Fig. 2(c)]. We observe small regions of the nanoribbon channel that have higher 2LA(M) intensities than the rest of the nanoribbon, as marked by "Spot 2" in Fig. 3(b). To examine these regions more closely, we investigate the TERS spectra of individual pixels within these areas in Fig. 3(c). Encouragingly, we do observe a substantially improved signal-to-noise ratio in the TERS spectra in Fig. 3(c), further validating that the cleaning procedure enabled high-quality samples and proper TERS enhancement compared to the nanoribbon from the first batch.

In Fig. 3(c), the 2LA(M) intensity sharply increases at the location of Spot 2 compared to the region marked "Spot 1," accompanied by redshifts in both 2LA(M) and A_1' peaks of 2.8 and 0.6 cm^{-1}, respectively, obtained from our Lorentzian peak fitting procedure. Such behavior may arise from growth inhomogeneities, which are either defects, grain boundaries, or multilayer islands.[37,38] Although we concurrently obtain topography in these measurements, the MoS_2

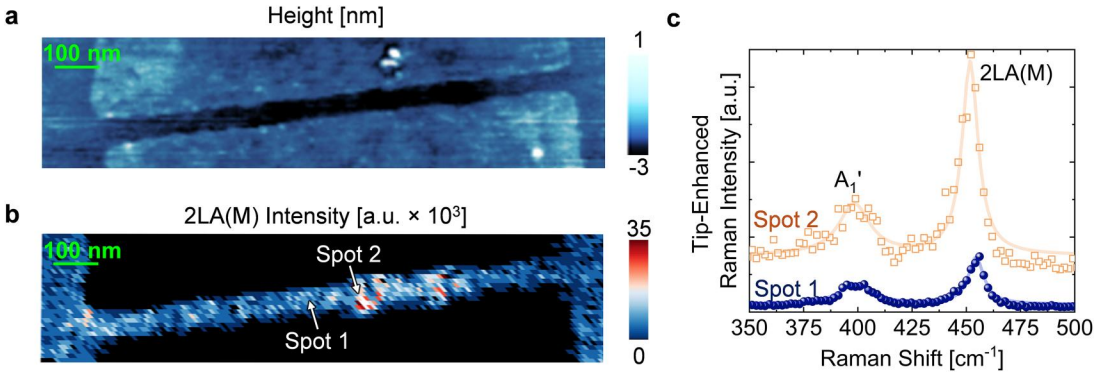

FIG. 3. TERS mapping of an MoS_2 nanoribbon transferred after additional vacuum annealing. (a) Topography and (b) TERS map of the same MoS_2 nanoribbon ($1400 \times 300\ nm^2$ map, 10 nm per pixel), displaying the intensity of the 2LA(M) mode. The intensity is highly uniform across the sample, owing to the complete removal of resist residue at the Au substrate/MoS_2 interface. Note that, in the topography map, the MoS_2 appears "sunk" into the Au film, which is used to remove the MoS_2 from its initial growth substrate. (c) TERS spectra of the nanoribbon center, labeled as Spots 1 and 2, from locations shown in panel (b). The spectra are normalized to the Rayleigh line, then shifted vertically for clarity. Symbols are experimental data, solid lines are Lorentzian peak fits.

nanoribbons are embedded inside the Au substrate (which is used to remove them from the SiO_2 growth substrate), making subtle thickness or grain boundary changes difficult to identify during the height mapping on the topmost MoS_2 surface. Regardless of the origin, these nanoscale inhomogeneities along the nanoribbons could lead to device-to-device variations in 2D devices, stressing the importance of improving the TMD monolayer crystal synthesis.

To convey the true potential of TERS imaging on nanoribbons, we also conduct a thorough analysis of our TERS mapping for the MoS_2 nanoribbon sample presented in Figs. 3 and 4. We systematically fit the A_1' and 2LA(M) peaks to one Lorentzian each, then minimize error between the measured spectra and the peak fits. Upon completing peak fitting [Figs. 4(a) and 4(b)], we can map the peak shifts from the growth inhomogeneities identified in Fig. 3. Thanks to the high spatial resolution of TERS (~10 nm), we may also investigate the effects of the nanoribbon edges on the TERS spectra, which we do by averaging the TERS spectra of ~10 pixels across the direction of each nanoribbon edge compared to the center of the channel itself [Fig. 4(c)]. Both edges do not exhibit distinguishable changes in full width at half maximum (FWHM) of the peaks, signaling that the nanoribbon edge quality is preserved, consistent with good transistor performance down to 25 nm nanoribbon widths.[32] However, the A_1' peak at the edges experiences a small redshift of $\sim 0.5\ cm^{-1}$, whereas the 2LA(M) peak remains unchanged. This redshift appears consistent with threshold voltage changes in devices with reduced widths, e.g., due to negative fixed charges[39] at the nanoribbon edges. This effect likely arises from fabrication and/or atmospheric exposure.[40] We emphasize that future TERS studies with higher spatial and spectral resolution on TMD nanoribbons are required to examine the fine peculiarities of the edges, especially because the A_1' peak splitting[35] cannot be resolved with the spectrometer grating and the instrumental broadening present in this study.

In summary, we show that gap-mode TERS imaging can serve as a prototype-stage technique for nanoscale quality control of

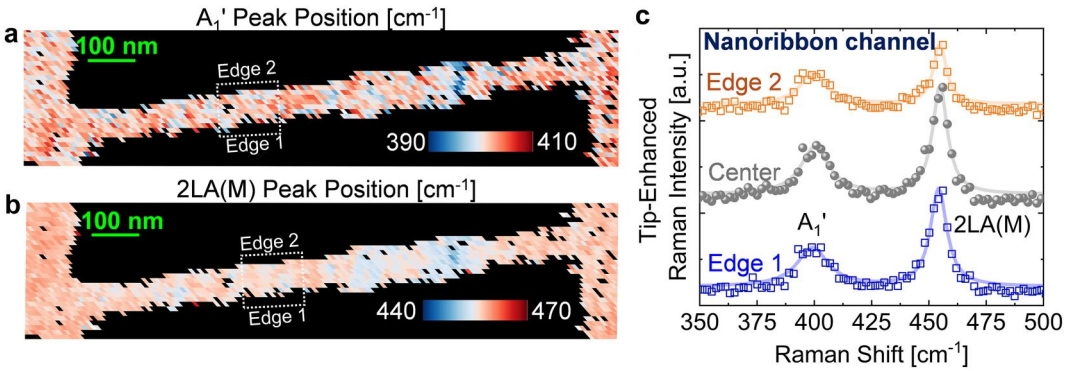

FIG. 4. Nanoscale Raman spectroscopic analysis on the vacuum-annealed MoS_2 nanoribbon. (a) Map of the A_1' peak position (in cm^{-1}) obtained by Lorentzian fitting of the TERS spectra at each pixel. (b) Map of the 2LA(M) peak position (in cm^{-1}) obtained from the same fits. (c) TERS spectra corresponding to the edges and nanoribbon center, where these spectra correspond to the dotted white box in the Raman maps presented in (a) and (b). The spectra are averages of ~10 pixels along the direction of the nanoribbon channel to improve signal-to-noise ratio and account for local variability. The spectra are normalized to the Rayleigh line, then shifted vertically for clarity. Symbols are experimental data, solid lines are Lorentzian peak fits.

monolayer MoS_2 nanoribbons with sub-100 nm widths. As a demonstration of the process-control capabilities of TERS, we observed that incomplete removal of electron-beam resist from solvent cleaning will cause significant reduction in TERS enhancement over contaminated regions. In contrast, nanoribbons with an additional vacuum annealing step exhibited a more uniform TERS response. We also identified sample inhomogeneities, likely arising from the growth process and some spectral signatures potentially consistent with fixed charge at the nanoribbon edges. These findings highlight the potential of TERS imaging as an ambient nanoscale characterization technique for the study and development of 2D-based nanoribbon devices.

Several authors were supported by SUPREME, a JUMP 2.0 center sponsored by the Semiconductor Research Corporation (SRC) and DARPA. T.P. would like to thank the National Science Foundation (NSF) MPS Ascend Postdoctoral Fellowship. A.E.O.P. acknowledges the Knut and Alice Wallenberg Foundation (Grant No. 2022.0374). T.P. and E.P. acknowledge Intel Corporation. K.N. acknowledges the Stanford Graduate Fellowship and the NSF Graduate Research Fellowship Program (Grant No. DGE-1656518). A.T.H. and A.J.M. acknowledge support from TSMC, and T.P., A.E.O.P., and E.P. acknowledge partial support from Samsung Electronics. Nanoribbon fabrication in this work was primarily performed at nano@stanford RRID:SCR_026695. E.P. and A.J.M. acknowledge the NSF FuSe2 Award No. 2425218.

AUTHOR DECLARATIONS

Conflict of Interest

The authors declare the following competing financial interests: HORIBA Scientific is the manufacturer of the equipment used in this study. Collaboration with industry and academia is a part of A.K.'s job responsibilities. The authors declare no additional conflicts of interest.

Author Contributions

Andrey Krayev: Conceptualization (equal); Data curation (lead); Writing – original draft (equal); Writing – review & editing (equal). **Tara Peña:** Conceptualization (equal); Formal analysis (lead); Methodology (equal); Writing – original draft (equal); Writing – review & editing (equal). **Anton E. O. Persson:** Methodology (equal); Writing – review & editing (equal). **Kathryn Neilson:** Methodology (equal); Writing – review & editing (supporting). **Anh Tuan Hoang:** Methodology (equal); Writing – review & editing (supporting). **Andrew J. Mannix:** Supervision (equal); Writing – review & editing (equal). **Eric Pop:** Conceptualization (equal); Supervision (lead); Writing – review & editing (equal).

DATA AVAILABILITY

The data that support the findings of this study are available from the corresponding author upon reasonable request.

REFERENCES

[1]J. E. Lee, G. Ahn, J. Shim, Y. S. Lee, and S. Ryu, "Optical separation of mechanical strain from charge doping in graphene," Nat. Commun. **3**, 1024 (2012).
[2]A. Michail, N. Delikoukos, J. Parthenios, C. Galiotis, and K. Papagelis, "Optical detection of strain and doping inhomogeneities in single layer MoS_2," Appl. Phys. Lett. **108**, 173102 (2016).
[3]C. A. Nattoo *et al.*, "Optoelectronic properties of atomic layer deposited and sputtered MoS_2 films," ACS Appl. Mater. Interfaces **17**, 47347–47354 (2025).
[4]T. Peña *et al.*, "Strain engineering 2D MoS_2 with thin film stress capping layers," 2D Mater. **8**, 045001 (2021).
[5]J. Lee, K. T. Crampton, N. Tallarida, and V. A. Apkarian, "Visualizing vibrational normal modes of a single molecule with atomically confined light," Nature **568**, 78–82 (2019).
[6]R. Zhang *et al.*, "Chemical mapping of a single molecule by plasmon-enhanced Raman scattering," Nature **498**, 82–86 (2013).
[7]S. A. Saunin *et al.*, "Systems and methods for non-destructive surface chemical analysis of samples," U.S. patent US2016/0341,764 A1 (2016).
[8]T. Zhang *et al.*, "Synthesis-related nanoscale defects in Mo-based janus monolayers revealed by cross-correlated AFM and TERS imaging," Small **21**, 2504742 (2025).
[9]Y. Zhang *et al.*, "Improving resolution in quantum subnanometre-gap tip-enhanced Raman nanoimaging," Sci. Rep. **6**, 25788 (2016).
[10]C. Kastl *et al.*, "The important role of water in growth of monolayer transition metal dichalcogenides," 2D Mater. **4**, 021024 (2017).
[11]K. K. H. Smithe *et al.*, "Nanoscale heterogeneities in monolayer $MoSe_2$ revealed by correlated scanning probe microscopy and tip-enhanced Raman spectroscopy," ACS Appl. Nano Mater. **1**, 572–579 (2018).
[12]B. M. Rajapakse *et al.*, "Tip-enhanced Raman scattering and near-field optical imaging of semiconducting monolayer and few-layer $MoTe_2$," Mater. Sci. Semicond. Process. **178**, 108442 (2024).
[13]D. Jariwala *et al.*, "Nanoscale doping heterogeneity in few-layer WSe_2 exfoliated onto noble metals revealed by correlated SPM TERS imaging," 2D Mater. **5**, 035003 (2018).
[14]F. Kargar *et al.*, "Metallic vs. semiconducting properties of quasi-one-dimensional tantalum selenide van der Waals nanoribbons," Nanoscale **14**, 6133–6143 (2022).
[15]T. P. Darlington *et al.*, "Imaging strain-localized excitons in nanoscale bubbles of monolayer WSe_2 at room temperature," Nat. Nanotechnol. **15**, 854–860 (2020).
[16]T. P. Darlington *et al.*, "Facile and quantitative estimation of strain in nanobubbles with arbitrary symmetry in 2D semiconductors verified using hyperspectral nano-optical imaging," J. Chem. Phys. **153**, 024702 (2020).
[17]T.-X. Huang *et al.*, "Probing the edge-related properties of atomically thin MoS_2 at nanoscale," Nat. Commun. **10**, 5544 (2019).
[18]S. Garg *et al.*, "Nanoscale Raman characterization of a 2D semiconductor lateral heterostructure interface," ACS Nano **16**, 340–350 (2022).
[19]A. Rodriguez, A. Krayev, M. Velický, O. Frank, and P. Z. El-Khoury, "Nano-optical visualization of interlayer interactions in WSe_2/WS_2 heterostructures," J. Phys. Chem. Lett. **13**, 5854–5859 (2022).
[20]A. Krayev *et al.*, "Comparable enhancement of TERS signals from WSe_2 on chromium and gold," J. Phys. Chem. C **124**, 8971–8977 (2020).
[21]A. Krayev *et al.*, "Dry transfer of van der Waals crystals to noble metal surfaces to enable characterization of buried interfaces," ACS Appl. Mater. Interfaces **11**, 38218–38225 (2019).
[22]Y. Liu *et al.*, "Promises and prospects of two-dimensional transistors," Nature **591**, 43–53 (2021).
[23]K. P. O'Brien *et al.*, "Process integration and future outlook of 2D transistors," Nat. Commun. **14**, 6400 (2023).
[24]C. D. English, G. Shine, V. E. Dorgan, K. C. Saraswat, and E. Pop, "Improved contacts to MoS_2 transistors by ultra-high vacuum metal deposition," Nano Lett. **16**, 3824–3830 (2016).
[25]C. J. Lockhart de la Rosa and G. S. Kar, "Introducing 2D-material based devices in the logic scaling roadmap," Semicond. Digest **6**, 17–21 (2024).
[26]W. Li *et al.*, "Approaching the quantum limit in two-dimensional semiconductor contacts," Nature **613**, 274–279 (2023).
[27]C. J. McClellan, E. Yalon, K. K. H. Smithe, S. V. Suryavanshi, and E. Pop, "High current density in monolayer MoS_2 doped by AlO_x," ACS Nano **15**, 1587–1596 (2021).

[28]A. T. Hoang *et al.*, "Low-temperature growth of MoS_2 on polymer and thin glass substrates for flexible electronics," Nat. Nanotechnol. **18**, 1439–1447 (2023).
[29]J. Zhu *et al.*, "Low-thermal-budget synthesis of monolayer molybdenum disulfide for silicon back-end-of-line integration on a 200 mm platform," Nat. Nanotechnol. **18**, 456–463 (2023).
[30]See https://irds.ieee.org/ for "IEEE international roadmap for devices and systems" (2025).
[31]X. Liu *et al.*, "Focused helium ion beam for direct patterning of monolayer MoS_2 nanoribbon field effect devices," Adv. Funct. Mater. **36**, e14880 (2025).
[32]T. Peña *et al.*, "Scaling nanoribbon transistors with monolayer transition metal dichalcogenides," Nat. Nanotechnol. (in press) (2026).
[33]K. K. H. Smithe, C. D. English, S. V. Suryavanshi, and E. Pop, "Intrinsic electrical transport and performance projections of synthetic monolayer MoS_2 devices," 2D Mater. **4**, 011009 (2017).
[34]A. Krayev *et al.*, "Excitation laser energy dependence of the gap-mode TERS spectra of WS_2 and MoS_2 on silver," ACS Photonics **12**, 1535–1544 (2025).
[35]M. Velický *et al.*, "Strain and charge doping fingerprints of the strong interaction between monolayer MoS_2 and gold," J. Phys. Chem. Lett. **11**, 6112–6118 (2020).
[36]S. Sun, D. T. N. Rathnayake, and Y. Guo, "Asymmetrical spectral continuum between anti-stokes and stokes scattering revealed in low-frequency surface-enhanced Raman spectroscopy," J. Phys. Chem. C **126**, 11193–11200 (2022).
[37]S.-L. Li *et al.*, "Quantitative Raman spectrum and reliable thickness identification for atomic layers on insulating substrates," ACS Nano **6**, 7381–7388 (2012).
[38]F. B. Sousa *et al.*, "Disentangling doping and strain effects at defects of grown MoS_2 monolayers with nano-optical spectroscopy," Nanoscale **16**, 12923–12933 (2024).
[39]B. Chakraborty *et al.*, "Symmetry-dependent phonon renormalization in monolayer MoS_2 transistor," Phys. Rev. B **85**, 161403 (2012).
[40]H. Liu, J. Gu, and P. D. Ye, "MoS_2 nanoribbon transistors: Transition from depletion mode to enhancement mode by channel-width trimming," IEEE Electron Device Lett. **33**, 1273–1275 (2012).